Astron. Astrophys. 332, 55–70 (1998)

ASTRONOMY
AND
ASTROPHYSICS

The Galactic X-ray halo

J. Pietz[1], **J. Kerp**[1], **P.M.W. Kalberla**[1], **W.B. Burton**[2], **Dap Hartmann**[2,3], **and U. Mebold**[1]

[1] Radioastronomisches Institut der Universität Bonn, Auf dem Hügel 71, D-53121 Bonn, Germany
[2] Sterrewacht Leiden, P.O. Box 9513, RA 2300 Leiden, The Netherlands
[3] Harvard-Smithsonian Center for Astrophysics, 60 Garden Street, Cambridge, MA 02138, USA

Received 27 February 1997 / Accepted 8 December 1997

Abstract. We analyzed the intensity distribution of the $3/4$ keV and $1/4$ keV diffuse soft X-ray background by correlating the *ROSAT* all-sky survey with the Leiden/Dwingeloo H I survey. We found that the $3/4$ keV and $1/4$ keV intensity distributions can be modelled by a contribution from an isothermal (kT = 0.135 keV) flattened X-ray halo superposed on the radiation from an extragalactic X-ray background. The exponential scale height of the X-ray halo is about 4.4 kpc and its radial scale length is about 15 kpc; the X-ray halo luminosity, $L_{\rm X}$, is about $7 \cdot 10^{39}$ erg s^{-1}.

Key words: Galaxy: halo – Galaxy: kinematics and dynamics – X-rays: ISM

1. Introduction

The X-ray background (XRB) can be conveniently subdivided into several energy ranges where the spectral properties and consequently also the origin of the X-ray radiation are different. At energies above 1 keV, the XRB radiation is dominantly of extragalactic origin (Fabian & Barcons 1992, Hasinger et al. 1993) and reveals, accordingly, an isotropic intensity distribution across the sky. Gendreau et al. (1995) used *ASCA* data to show that the extragalactic XRB spectrum between 1 and 7 keV can be approximated by a power-law with a photon index, Γ, of about -1.4. Moreover, they found evidence for excess X-ray emission, deviating from this power-law, at energies below 1 keV. Gendreau et al. (1995) fit this excess soft X-ray radiation using a thermal plasma with a temperature in the range kT = 0.14–0.16 keV. Soltan et al. (1996) also found evidence for a change in the spectral properties of the XRB below 1 keV in an autocorrelation analysis of the *ROSAT* all-sky survey. Nousek et al. (1982) had earlier come to similar conclusions by analyzing X-ray data obtained with non-imaging X-ray detectors; they favored (in particular for the $3/4$ keV range) an XRB model consisting of two components, one extragalactic and one with its origin in the halo of our Galaxy. The X-ray radiation of both contributions is attenuated by photoelectric absorption caused by the intervening interstellar matter distributed along the line of sight. However, the X-ray data analyzed by Nousek et al. (1982) did not allow them to distinguish in detail between different models of the XRB.

Modeling the XRB is more complicated in the $1/4$ keV energy range than at higher photon energies. Roughly half of the observed $1/4$ keV X-ray radiation can be attributed to thermal-plasma emission originating within the low-volume density environment surrounding the Sun, sometimes called the Local Hot Bubble (LHB; for a review see McCammon & Sanders 1990). The remaining half of the soft X-ray emission results from the superposition of the extragalactic XRB upon the diffuse galactic X-ray radiation arising at large distances in our own Galaxy (see Kerp et al. 1997).

In this paper we investigate the distant diffuse galactic soft X-ray radiation by correlating two new data sets: the Leiden/Dwingeloo H I 21-cm line survey (Hartmann & Burton 1997) and the public *ROSAT* all-sky survey (RASS, Snowden et al. 1995) covering the $3/4$ keV and $1/4$ keV energy ranges. Our aim is to improve the earlier analysis of Nousek et al. (1982) by analyzing more modern X-ray data obtained with an imaging X-ray detector, and by correlating these data with the new H I data, in the realization that the distribution of the neutral interstellar gas largely determines the appearance of the soft X-ray sky. The data sets are briefly described in Sect. 2.

The RASS data are supplemented here by selected pointed PSPC observations, in order to address the contribution of the point sources to the XRB maps. Moreover, the PSPC pointings are used to derive the spectral composition of the XRB (Sect. 3). The spectral properties so determined are then used to solve the soft X-ray radiation transport equation for the $3/4$ keV and for the $1/4$ keV RASS data (Sect. 4). A modified isothermal flattened-halo X-ray model is presented by incorporating a radial scale length (Sect. 5). We compare this new galactic X-ray halo model with the $1/4$ keV RASS data in Sect. 6. We summarize our results in Sect. 7.

Send offprint requests to: P.M.W. Kalberla

2. Data

2.1. Soft X-ray data

A detailed description of the RASS data and their reduction has been given by Snowden et al. (1995). The public RASS XRB maps are binned into three energy bands: the $1/4$ keV band (pulse-height invariant energy, PI, channels $11-41$), the $3/4$ keV band (PI channels $52-91$), and the 1.5 keV band (PI channels $92-201$). The angular resolution is about 2°. The integration time varies appreciably: from several thousands of seconds for directions near the ecliptic poles, down to several tens of seconds near the ecliptic equator.

The PSPC pointed observations have been corrected for various non-cosmic background components (Snowden et al. 1994). The short-term enhancements were excluded by selecting nighttime periods of the *ROSAT* orbits in the $3/4$ keV band. The particle background was subtracted using the method described by Plucinsky et al. (1993). Possible long-term enhancement contaminations were identified by comparing the pointed-observation count rates with the RASS count rates, and by comparing the count rates in positional overlapping areas of different pointings.

2.2. H I data

A survey of the neutral hydrogen in our Galaxy at $\delta > -30^\circ$ was recently completed using the 25-m radio telescope in Dwingeloo. The Leiden/Dwingeloo survey (Hartmann 1994, Hartmann & Burton 1997) has a velocity coverage ranging from $-450\,\mathrm{km\,s^{-1}}$ to $+400\,\mathrm{km\,s^{-1}}$, an angular sampling of $0\fdg5$, and an rms intensity limit of 0.07 K; the survey has been corrected for stray radiation (Hartmann et al. 1996). This survey provides the most precise H I column densities of the northern sky available.

For analysis of the H I column density distribution in certain limited fields at higher angular resolution we obtained H I 21-cm spectra with the 100-m radio telescope in Effelsberg. The principles of the reduction of Effelsberg H I spectra have been described by Herbstmeier et al. (1996). The spectra in the selected fields have an angular resolution of $9'$, a velocity resolution of $1.2\,\mathrm{km\,s^{-1}}$, and an rms level of 0.2 K.

3. Spectral components of the XRB

In this section we decompose the XRB radiation into its individual spectral components. As mentioned in the introduction, the excess soft X-ray emission below 1 keV can be explained by absorbed background radiation emitted by thermal plasma in the temperature range of $kT = 0.14$–0.16 keV (Gendreau et al. 1995). Rocchia et al. (1984) found evidence for line emission in XRB spectra, supporting the assumption that a significant part of the XRB is of thermal origin.

To investigate the spectral composition of this emission we need to use at least three source terms when fitting the PSPC X-ray spectra: the first of these terms represents the contribution from a local foreground gas, denoted as $C_{\rm fg}$; the second term, $C_{\rm extra}$, represents the extragalactic XRB radiation; and the third term, $C_{\rm dist\,Gal}$, represents the distant galactic X-ray plasma in our Galaxy.

Table 1. Central positions as well as the total and analyzed exposure times of the PSPC pointed observations near $(l,b) \sim (90^\circ, 60^\circ)$. These PSPC observations were analyzed to disclose the spectral composition of the XRB. The column $t_{\rm int}$ gives the available total integration time; $t_{\rm used}$ denotes the analyzed time after correction for the non-cosmic backgrounds.

Sequence ID	l	b	$t_{\rm int}$[s]	$t_{\rm used}$ [s]
900584p	$85\fdg0$	$59\fdg0$	7905	7740
600448p	$87\fdg0$	$60\fdg6$	12862	11615
701370p	$86\fdg6$	$61\fdg8$	6780	6033
701408p	$90\fdg0$	$57\fdg5$	6844	6716

In order to evaluate the physical parameters of the different XRB components we selected several high-galactic-latitude PSPC pointings near $(l,b) \sim (90^\circ, 60^\circ)$ (Table 1). The selected PSPC pointings cover an H I column-density range of $0.8{\cdot}10^{20}\,\mathrm{cm^{-2}} \leq N_{\rm HI} \leq 6{\cdot}10^{20}\,\mathrm{cm^{-2}}$. In accordance with the accumulating evidence that the distribution of the soft X-ray sky is anti-correlated to the H I column density distribution (see Kerp et al. 1997), a high H I column-density contrast yields a high X-ray intensity contrast. The selected pointings avoid areas close to the well-known radio-continuum loops (e.g. Berkhuijsen 1971).

Fits to *ROSAT* X-ray spectra allow separating the thermal and the extragalactic XRB components superposed in the broad energy bands of the $1/4$ keV and $3/4$ keV RASS data. Furthermore, this spectral analysis constrains the temperature of the distant galactic X-ray plasma.

In order to determine the distribution of absorbing column densities in detail we observed the H I distribution with the Effelsberg telescope, selecting several areas within the individual *ROSAT* pointings optimized to cover a large range of H I column densities. Since no ^{12}CO ($1 \rightarrow 0$) emission is detected towards the cloud in question (Heiles et al. 1988, Reach et al. 1994), and since the observed H I column-density distribution reproduces the observed IRAS 100-μm intensity variations, at least down to a $9'$ angular resolution, molecular gas as an additional X-ray absorber can be neglected.

We modelled the radiation transfer of X-ray absorbing and emitting gas according to the scheme:

$$\text{extragalactic and distant galactic XRB emission} \rightarrow \text{absorber} \\ \rightarrow \text{local X-ray plasma} \rightarrow \text{observer}$$

For the spectral fitting procedure we used the Mewe-Kaastra (MK) X-ray plasma code (Mewe et al. 1985) and the photoelectric absorption cross sections of Morrison & McCammon (1983). We fit three source components to the X-ray spectra: a foreground MK plasma, an absorbed distant MK plasma, and an absorbed extragalactic photon power law (PL). To minimize the number of free parameters, we fixed the foreground plasma

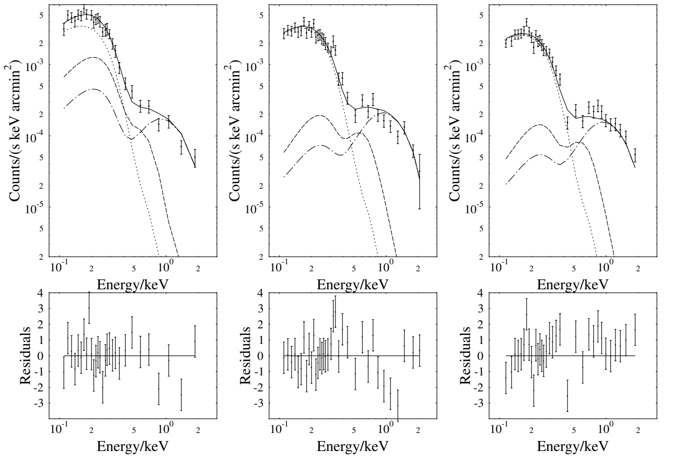

Fig. 1. X-ray spectra derived from the PSPC pointed observations (Table 1). The X-ray absorbing column density varies from $N_{\rm HI}$ = $1.0{\cdot}10^{20}\,{\rm cm}^{-2}$ at $(l, b) = (91\overset{\circ}{.}3, 57\overset{\circ}{.}9)$ (*left*), to $N_{\rm HI} = 2.2{\cdot}10^{20}\,{\rm cm}^{-2}$ at $(86\overset{\circ}{.}1, 58\overset{\circ}{.}7)$ (*center*), and then up to $N_{\rm HI}$ = $5.2{\cdot}10^{20}\,{\rm cm}^{-2}$ at $(85\overset{\circ}{.}8, 59\overset{\circ}{.}5)$ (*right*). The individual X-ray spectra were approximated by a model composed of three X-ray source components. A foreground X-ray component represents the local hot interstellar medium with a plasma temperature of about kT = 0.08 keV (dotted line); a distant plasma component has a temperature of about kT = 0.135 keV (dashed line); and the extragalactic X-ray background radiation is represented by a power-law X-ray spectrum with $E^{-1.4}$ (Gendreau et al. 1995, dot-dashed line). All spectra were fitted with the *same* parameterization of the X-ray source components: we found a consistent solution for the XRB spectrum (solid line) over this large range of absorbing column densities observed towards high galactic latitudes.

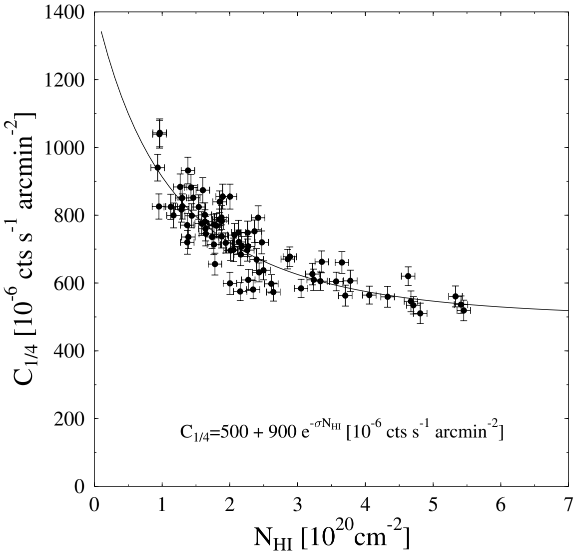

Fig. 2. Anti-correlation diagram of 1/4 keV count rate versus the total H I column density for the pointed PSPC observations (Table 1). The line indicates the best-fit solution for a two-source component model with a foreground count rate of $C^{\rm scatter}_{1/4,{\rm fg}}$ = $500{\cdot}10^{-6}\,{\rm cts\,s^{-1}\,arcmin^{-2}}$ and a background rate of $C^{\rm scatter}_{1/4,{\rm bg}}$ = $900{\cdot}10^{-6}\,{\rm cts\,s^{-1}\,arcmin^{-2}}$. Within the *ROSAT* 1/4 keV band the transmission of the distant plasma and of the extragalactic background photons differ by only about 7%; we can therefore approximate the superposition of both X-ray source terms by a single component. Thus, the two-component model fits the observed situation well.

temperature to kT = (0.08 ± 0.01) keV and provided an ubiquitous absorbing column density of $N_{\rm HI} = 1 \cdot 10^{19}\,{\rm cm}^{-2}$ (Kerp 1994). The temperature of the local X-ray plasma is derived from the X-ray band ratio of the R1 (PI channels 11 − 19) and R2 energy band (PI channels 20 − 41), obtained towards high column density ($N_{\rm HI} \geq 4.5 \cdot 10^{20}\,{\rm cm}^{-2}$) areas, where the ISM is optically thick for the background 1/4 keV emission. Our temperature value is consistent with other publications (e.g. Sidher et al. 1996). An extragalactic power-law photon index of $\Gamma = -1.4$ was used; this choice of the spectral index follows Gendreau et al. (1995) but is also consistent with the results of Almaini et al. (1996), who found that the photon index decreases towards fainter X-ray point source fluxes: $\Gamma = -1.5 \pm 0.1$ at $F_{\rm X} = 4 \cdot 10^{-15}\,{\rm erg\,s^{-1}\,cm^{-2}}$. Because our analysis deals with *ROSAT* PSPC data which have an average X-ray flux level fainter than $F_{\rm X} = 2 \cdot 10^{-15}\,{\rm erg\,s^{-1}\,cm^{-2}}$, we adopt the power-law index as given by Gendreau et al. (1995). We optimized the spectral fitting procedure to fit simultaneously all three X-ray spectra with the same emission measures as well as with the same plasma temperatures. We stress that the differences between the X-ray spectra shown in Fig. 1 follow solely from the very different H I column densities attenuating the distant X-ray components.

As the best-fit temperature for the distant X-ray plasma we obtained kT = 0.135 ±0.05 keV, a value in agreement with the results of others (e.g. Kerp 1994, Sidher et al. 1996) and close to the low X-ray plasma temperature range found by Gendreau et al.(1995).

The derived X-ray plasma parameters were additionally checked using an anti-correlation analysis comparing the 1/4 keV radiation and the H I column density. We plotted the 1/4 keV count rate $C_{1/4}$ versus $N_{\rm HI}$ in Fig. 2 and fitted this scatter diagram by a model based on two X-ray source components: a foreground count rate $C^{\rm scatter}_{1/4,{\rm fg}}$ and an absorbed background count rate $C^{\rm scatter}_{1/4,{\rm bg}}$.

This approach is justified because the absorption factors of the thermal plasma and the power-law spectra, ${\rm e}^{-\sigma(T,N_{\rm HI})N_{\rm HI}}$, are equal within the statistical uncertainties of the X-ray data. Therefore, we evaluate the sum of the extragalactic background component, $C^{\rm scatter}_{1/4,{\rm extra}}$, and the thermal galactic component, $C^{\rm scatter}_{1/4,{\rm dist\,Gal}}$. This sum of both count rates, $C^{\rm scatter}_{1/4,{\rm bg}}$, corresponds to the emission measure of the distant plasma and gives the amplitude of the power-law component in the spectral fits. Therefore, the radiation transport equation for the 1/4 keV energy range can be simplified to:

$$C^{\rm scatter}_{1/4} = C^{\rm scatter}_{1/4,{\rm fg}} + C^{\rm scatter}_{1/4,{\rm bg}} \cdot e^{-\sigma_{1/4}(N_{\rm HI}) \cdot N_{\rm HI}} \quad (1)$$

The resulting intensities are (see Fig. 2):

$$C^{\rm scatter}_{1/4,{\rm fg}} = (500 \pm 10) \cdot 10^{-6}\,{\rm cts\,s^{-1}\,arcmin^{-2}} \quad (2)$$

$$C^{\mathrm{scatter}}_{1/4,\mathrm{bg}} = (900 \pm 40) \cdot 10^{-6}\,\mathrm{cts\,s^{-1}\,arcmin^{-2}} \quad (3)$$

These values are consistent with the mean intensities derived from spectral fits converted into count rates of the 1/4 keV band: $C^{\mathrm{spec}}_{1/4,\mathrm{fg}} = (510 \pm 30)\cdot 10^{-6}\,\mathrm{cts\,s^{-1}\,arcmin^{-2}}$ for the foreground component, and $C^{\mathrm{spec}}_{1/4,\mathrm{bg}} = (800 \pm 100)\cdot 10^{-6}\,\mathrm{cts\,s^{-1}\,arcmin^{-2}}$ for the sum of both distant XRB components. This quantitative agreement between the spectral fits and the scatter-diagram analysis indicates that the derived emission measures and plasma temperatures are well determined.

In the above, we have neglected the influence of the ionized interstellar medium on the photoelectric absorption of the X-ray radiation. If we assume that the ionized galactic hydrogen is located in front of the distant galactic XRB component, a mean absorbing column density of $N_{\mathrm{H^+}} \simeq 0.8\cdot 10^{20}\,\mathrm{cm^{-2}}$ has to be added as additional absorber towards the field of interest (see Reynolds 1991). Using the mean photoelectric absorption cross section of the ionized gas layer given by Snowden et al. (1994b) and the anti-correlation method described above, we obtain values of $C^{\mathrm{scatter}}_{1/4,\mathrm{fg}} = (505 \pm 10) \cdot 10^{-6}\,\mathrm{cts\,s^{-1}\,arcmin^{-2}}$ and $C^{\mathrm{scatter}}_{1/4,\mathrm{bg}} = (1400 \pm 65) \cdot 10^{-6}\,\mathrm{cts\,s^{-1}\,arcmin^{-2}}$.

The 3/4 keV count rates are much less influenced than the 1/4 keV count rates by ionized gas with column densities $N_{\mathrm{H^+}} < 1\cdot 10^{20}\,\mathrm{cm^{-2}}$. Therefore, the ratio between the 3/4 keV background count rate and the corresponding 1/4 keV count rate would increase if $\mathrm{H^+}$ were added to the absorbing column density. Since the power-law contribution is determined by the high-energy part of the spectrum, this yields a slightly cooler X-ray background plasma temperature as evaluated by the spectral fitting procedure above. Based on this consideration we estimate that the distant galactic X-ray plasma temperature is $kT = 0.13-0.14\,\mathrm{keV}$.

Using this temperature we can now extrapolate the intensity values of the 1/4 keV scatter analysis to the 3/4 keV energy band and can disentangle the contributions of $C_{3/4,\mathrm{extra}}$ and of $C_{3/4,\mathrm{dist\,Gal}}$ to $C_{3/4,\mathrm{bg}}$. Approximately 35% of the total unabsorbed 3/4 keV count rate, $C_{3/4,\mathrm{bg}} = 110 \cdot 10^{-6}\,\mathrm{cts\,s^{-1}\,arcmin^{-2}}$, is caused by the background plasma component. Consequently, the contribution of the extragalactic XRB component is about $C_{3/4,\mathrm{extra}} = 70\cdot 10^{-6}\,\mathrm{cts\,s^{-1}\,arcmin^{-2}}$, consistent with the spectral fitting results of $C_{3/4,\mathrm{extra}} = (70 \pm 10) \cdot 10^{-6}\,\mathrm{cts\,s^{-1}\,arcmin^{-2}}$. In the 1.5 keV energy range, less than < 5% of the total observed radiation can be attributed to the distant galactic plasma component.

4. The 3/4 keV RASS data

In our analysis of the RASS data we subdivided the sky into galactic latitude strips of 10° width. Fig. 3 shows, for example, the RASS 3/4 keV and 1.5 keV data and the Leiden/Dwingeloo H I data for two strips: $b = 40°$ to $50°$ (*upper* and $b = -30°$ to $-20°$ *lower*). Before analyzing the intensity distribution of the 3/4 keV count rate (Sects. 4.3 and 4.4), we first have to account for the contamination of the RASS data by point sources in the diffuse XRB maps (Sect. 4.1). Furthermore, we have to exclude individual galactic X-ray features such as Loop I (e.g. Egger & Aschenbach 1995) and the Orion-Eridanus Bubble (e.g. Brown et al. 1995 and Guo et al. 1995, Sect. 4.2).

4.1. Residual contamination of the RASS data

The 3/4 keV map shown by Snowden et al. (1995) shows residual scanning effects, reaching X-ray intensities of about $50\cdot 10^{-6}\,\mathrm{cts\,s^{-1}\,arcmin^{-2}}$ relative to the neighbouring areas. The comparison of the 3/4 keV and 1.5 keV latitude strips shown in Fig. 3 reveals that the scatter of the data points is larger in the 1.5 keV band than in the 3/4 keV one. Since the contribution of the extragalactic XRB resulting from the superposition of X-ray point sources is significantly larger at 1.5 keV than at 3/4 keV (Sect. 3), we attribute this enhanced scatter to the presence of X-ray point sources which have not been subtracted. Since the count rates of the 3/4 keV and 1.5 keV energy bands are almost the same, the difference in scatter is *not* caused by photon statistics.

Before converting our spectral fit results to the RASS data we have to consider the cumulative effect of the not-removed point sources on the survey data. To determine the level of the extragalactic XRB in the 3/4 keV RASS data we analyzed 22 individual PSPC pointed observations, distributed in the range $l = 40° - 140°$, $b = -60°$ to $+80°$. Towards sky areas where these pointed PSPC data showed no significantly-detected point sources we evaluated the count rate of the XRB in the 3/4 keV and 1.5 keV energy bands. Accounting for the lower angular resolution of the RASS data we evaluate a constant count–rate offset between the pointed PSPC data and the RASS maps. The RASS data reveal a count-rate offset of $\Delta C_{3/4} = 20-30\cdot 10^{-6}\,\mathrm{cts\,s^{-1}\,arcmin^{-2}}$, generally higher than that of the pointed observations. This enhanced XRB level of the RASS data relative to the PSPC pointings, can most likely attributed to not-subtracted point sources. Due to the angular smoothing procedure applied to the RASS data we can assume that this count-rate offset is constant across the sky. Henceforward we use $\Delta C_{3/4} = 25\cdot 10^{-6}\,\mathrm{cts\,s^{-1}\,arcmin^{-2}}$ to represent the constant XRB residual point-source offset for the RASS data relative to the pointed PSPC observation analysis.

Now we can evaluate the 3/4 keV XRB intensity level for the RASS. As shown in Sect. 3, the pointed PSPC data give $C_{3/4,\mathrm{extra}} = 70\cdot 10^{-6}\,\mathrm{cts\,s^{-1}\,arcmin^{-2}}$. We add now the residual-point-source intensity level, $\Delta C_{3/4}$, and arrive thus at $C_{3/4,\mathrm{extra}} = 95\cdot 10^{-6}\,\mathrm{cts\,s^{-1}\,arcmin^{-2}}$ for the RASS data set.

Before starting the analysis of the distant galactic XRB component in the 3/4 keV RASS data, individual extended X-ray features need to be excluded from further analysis, since we are interested in the smooth, undisturbed soft XRB distribution. Fig. 3 shows that in the general direction of the inner Galaxy ($l \sim 270°$ to $50°$) the 3/4 keV and 1.5 keV count rates are anomalously high. Most of this excess emission is associated with the Loop I shell (e.g. Egger & Aschenbach 1995). A second component may be attributable to emission from the galactic bulge itself. Another prominent X-ray region is located in

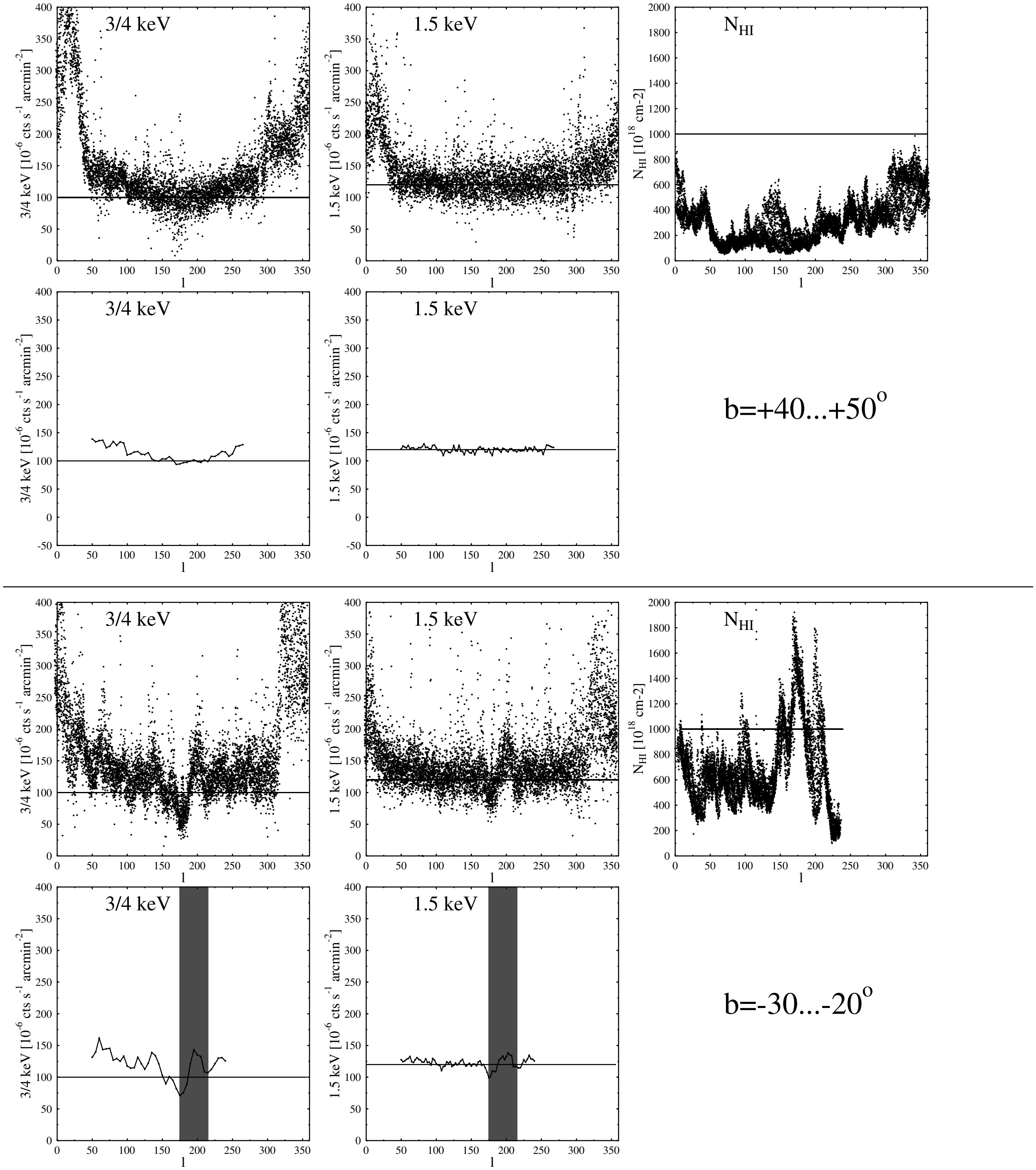

Fig. 3. Two examples of the analyzed galactic latitude strips with $\Delta b = 10°$ width. In the upper panel the galactic latitude range between $b = 40°$ and $50°$ is shown; the lower panel represents the latitudes between $b = -30°$ and $-20°$. The upper row in each panel shows the raw data for the $3/4$ keV (*left*) and 1.5 keV RASS (*middle*) energy bands and the corresponding total H I column densities (*right*). The scatter of the X-ray raw-data points stems from photon statistics and from the presence of X-ray point sources not subtracted from the XRB maps. In the lower row of each panel, the X-ray data is smoothed over galactic longitude, to a resolution of $\Delta l = 5°$, after removing the brightest point sources. The smoothed data sets did not contain the X-ray contributions for Loop I or the Orion-Eridanus Bubble (grey-shaded area), which are visible as bright X-ray features in the raw $3/4$ keV and 1.5 keV maps.

the general direction of the galactic anticenter, at $l \sim 170°$ to 220°, namely the Orion-Eridanus Bubble (e.g. Brown et al. 1995, Guo et al. 1995). In the following, Loop I and/or the galactic bulge region will be masked out completely, whereas the Orion/Eridanus Bubble will be marked by a grey area in the diagrams (see Fig. 3).

4.2. *Dependence of the* $3/4$ *keV amplitudes on galactic longitude*

The variation of the $3/4$ keV and 1.5 keV count rates with galactic longitude (Fig. 3) suggests — if the individual features mentioned in the previous section are ignored — that the 1.5 keV count rate is constant, whereas the $3/4$ keV rate varies with longitude. The lowest $3/4$ keV count rates are reached at $l \sim 180°$, suggesting a galactic origin for a significant fraction of the $3/4$ keV radiation.

The foreground X-ray gas with a temperature of $kT \sim 0.08$ keV (Kerp 1994, Sidher et al. 1996) contributes only negligibly to the total $3/4$ keV count rate. This conclusion is supported by an anti-correlation analysis of the $3/4$ keV data of PSPC pointings toward $(l, b) \sim (90°, 60°)$, where we obtain a $3/4$ keV foreground component of $C_{3/4,\mathrm{fg}} = (7 \pm 30)\cdot 10^{-6}$ cts s^{-1} arcmin^{-2} . Moreover, since more than 85% of the total H I column density is located below $|z| < 400$ pc (e.g. Lockman & Gehman 1991), we conclude that a substantial portion of the $3/4$ keV radiation originates beyond the bulk of neutral hydrogen towards high galactic latitudes. Photoelectric absorption by the interstellar matter on the line of sight thus has to be taken into account.

Towards high latitudes the N_{HI} is typically about $1 - 2\cdot 10^{20}\mathrm{cm}^{-2}$; therefore the attenuation of the $3/4$ keV XRB is about 12%. To account for the observed intensity contrast (see e.g. Fig. 5, $|b| = 25°$) between the galactic anticenter region and the directions towards the galactic center we need a column-density contrast of $\Delta N_{\mathrm{HI}} \simeq 10 \cdot 10^{20}\mathrm{cm}^{-2}$ across large angular scales. Such a large contrast is not observed for the warm H I layer (Dickey & Lockman 1990) which accounts dominantly for the photoelectric absorption (Kerp & Pietz 1996). Therefore the photoelectric absorption traced by H I cannot account for the observed $3/4$ keV intensity variation.

Absorption across large angular scales by molecular hydrogen can be neglected, because at high latitudes ($|b| > 20°$) the surface filling factor of H_2 is only about 0.005 (e.g. Magnani et al. 1996). The H^+ layer (Reynolds 1991) can also not account for the $3/4$ keV intensity variation because its maximum column density is about $N_{\mathrm{H}^+} \le 1 \cdot 10^{20}$ cm^{-2} and consequently absorbs the X-ray radiation insignificantly in comparison to the H I .

We conclude that the observed variation of $3/4$ keV intensities with galactic longitude is *not* caused by photoelectric absorption. Therefore, the isotropic intensity distribution of the extragalactic XRB is not the source of the observed intensity variation with galactic longitude. Most probably the observed $3/4$ keV intensity variation is caused by the intensity variation of the distant galactic XRB source. Towards the galactic center the distant galactic XRB source is bright while towards the outskirts of the galactic disk the intensity decreases.

In view of the above we can simplify the radiation transport equation for the $3/4$ keV energy range to:

$$C_{3/4} = C_{3/4,\mathrm{MK}} \cdot e^{-\sigma(\mathrm{MK})N_{\mathrm{HI}}} + C_{3/4,\mathrm{PL}} \cdot e^{-\sigma(\mathrm{PL})N_{\mathrm{HI}}} \quad (4)$$

where σ(MK) and σ(PL) denote the effective photoelectric absorption cross sections.

5. Distribution of the thermal $3/4$ keV XRB

In Sect. 4 we found evidence that the observed intensity variation of the $3/4$ keV XRB radiation is a function of galactic longitude. Since the differential photoelectric absorption cannot cause the apparent intensity variation between the galactic center and anticenter we conclude that the distant galactic XRB plasma component is the source of the intensity variation.

It is important to establish the distribution of the distant X-ray plasma located beyond the bulk of the galactic neutral hydrogen layer. Nousek et al. (1982) confronted three different models with $3/4$ keV observations which had been obtained on Aerobee rocket flights:

1. An isotropic background component $C_{3/4,\mathrm{bg,iso}}$ affected by absorption plus a local unabsorbed foreground component $C_{3/4,\mathrm{fg}}$:
$$C_{3/4} = C_{3/4,\mathrm{fg}} + C_{3/4,\mathrm{bg,iso}} \cdot e^{-\sigma N_{\mathrm{H}}} \quad (5)$$
2. A layer parallel to the galactic plane $C_{3/4,\mathrm{bg,disk}}$ plus an extragalactic isotropic component $C_{\mathrm{bg,iso}}$, both absorbed by neutral matter in the Galaxy:
$$C_{3/4} = \left(C_{3/4,\mathrm{bg,disk}}/\sin|b| + C_{3/4,\mathrm{bg,iso}}\right) e^{-\sigma N_{\mathrm{H}}} \quad (6)$$
3. A spherical galactic halo model as an uniformly emitting sphere $C_{3/4,\mathrm{sphere}}$ affected by absorption:
$$C_{3/4} = C_{3/4,\mathrm{sphere}} \left(\cos(\theta) + \left(\rho^2 - \sin^2(\theta)\right)^{1/2}\right) e^{-\sigma N_{\mathrm{H}}} \quad (7)$$
where $\rho = R_{\mathrm{halo}}/R_{\odot} > 1$ is the radius of the halo in units of the solar galactocentric distance and $\cos(\theta) = \cos(l)\cos(b)$.

Nousek et al. (1982) found that their models 1 and 2 gave acceptable fits to the X-ray data available at that time. They concluded in favor of a disk-like galactic halo (model 2), mainly because such a model is easier to understand in a physical context.

In the following we perform an analysis similar to that of Nousek et al. (1982) using the RASS and the Leiden/Dwingeloo H I data. With the new H I and X-ray data it is possible to constrain the models more strongly.

5.1. *Modeling the* $3/4$ *keV XRB*

We start the analysis with model 1. Based on the results given in Sect. 3 and Sect. 4, we assume that the 3/4 keV foreground component is $C_{3/4,\mathrm{fg}} \approx 0$. The extragalactic XRB component is $C_{3/4,\mathrm{PL}} \approx 95\cdot 10^{-6}$ cts s^{-1} arcmin^{-2} and

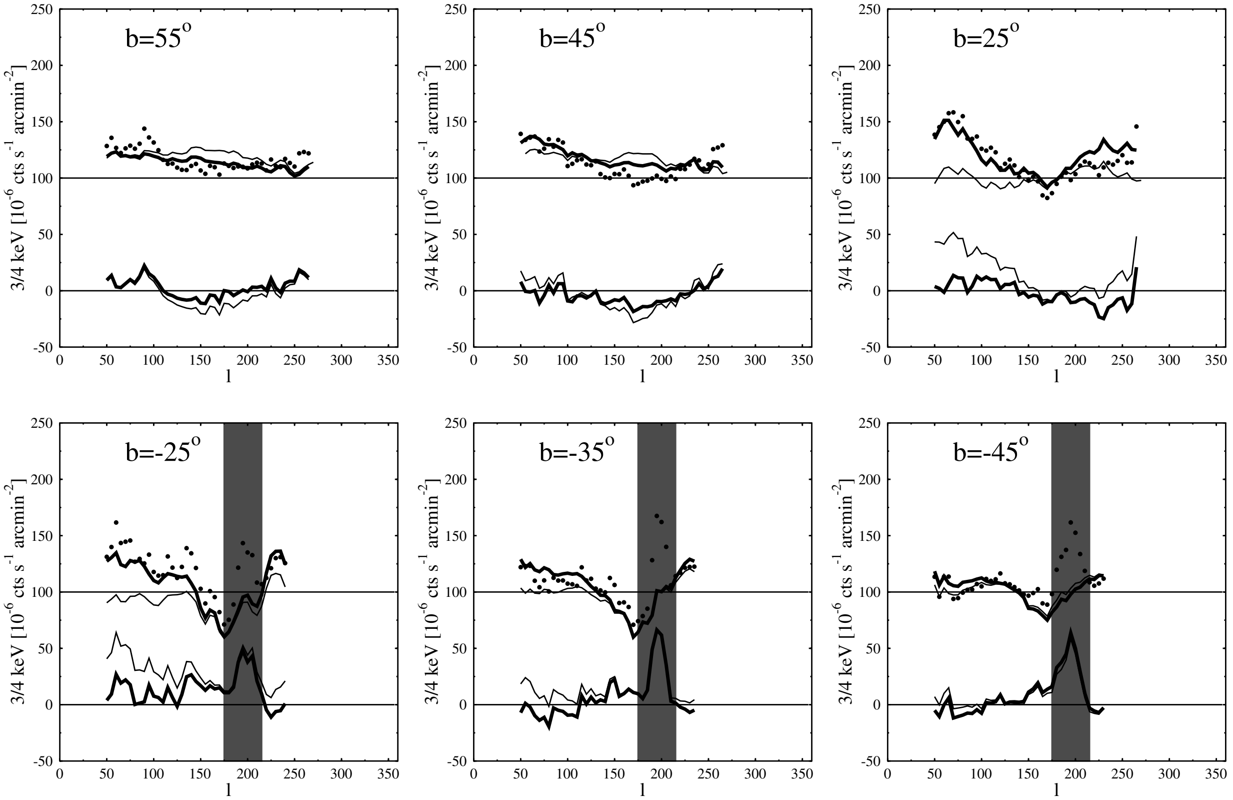

Fig. 4. Comparison of the observed 3/4 keV count rates (*points*) with the halo model 1 (isotropic XRB intensity distribution, *thin line*) for selected latitude strips towards the northern (*upper panel*) and southern galactic hemispheres (*lower panel*). The isotropic count rate $C_{3/4,\mathrm{bg,iso}}$ is the superposition of the extragalactic component with an intensity of $C_{3/4,\mathrm{extra}} = 95{\cdot}10^{-6}$ cts s^{-1} arcmin^{-2} and a distant X-ray plasma component with a temperature of k$T = 0.135$ keV and an X-ray intensity of $C_{3/4,\mathrm{MK}} = 55{\cdot}10^{-6}$ cts s^{-1} arcmin^{-2} . Both components are absorbed by all neutral matter distributed along the line of sight. The shaded area marks the position of the Orion-Eridanus Bubble. The thick line represents an intensity-variable plasma component as a function of galactic longitude in addition to the constant extragalactic XRB. At $|b| \sim 25°$ the thermal component decreases linearly from $150{\cdot}10^{-6}$ cts s^{-1} arcmin^{-2} ($l \sim 50°$) down to $100{\cdot}10^{-6}$ cts s^{-1} arcmin^{-2} ($l \sim 180°$). The amplitude of the 3/4 keV XRB intensity variation decreases with increasing latitude. The difference between the observed 3/4 keV intensity distribution and the models is plotted in the lower half of each diagram. The longitude-dependent plasma model fits the observations best.

the distant galactic XRB plasma count rate is $C_{3/4,\mathrm{MK}} \approx 40{\cdot}10^{-6}$ cts s^{-1} arcmin^{-2} in the direction of $(l, b) \sim (90°, 60°)$.

Using these values we calculate the expected count rate distribution using Eq. (5) and compare the count rates with the observations (thin lines in Fig. 4). On small angular scales of $\Delta l \leq 20°$, the 3/4 keV intensity distribution can be reproduced. For example, the deep X-ray absorption minima near $(l, b) = (155°, -25°)$, $(175°, -25°)$, and $(175°, -35°)$ close to the Orion-Eridanus Bubble can be modelled, demonstrating that the fraction of the H I column to the total absorbing column density is sufficient to model the absorption of the 3/4 keV radiation even in this molecular-gas-rich area. Even the humps in Fig. 5 between $l = 75°$ and $l = 175°$ at $b = -35°$ and $b = -45°$ are predicted by the model. This demonstrates that Eq. (4) is meaningful in describing the observed 3/4 keV count rate distribution on angular scales of $\Delta l < 20°$ towards the high-latitude sky.

Nevertheless, deviations of the observed count rates from the modelled 3/4 keV count rates exist on larger angular scales. All 3/4 keV latitude slices reveal a count rate minimum in the direction of the galactic anticenter (e.g. Fig. 4, $b = 40° - 50°$). The intensity contrast between the galactic anticenter region and the neighbouring longitudes decreases with increasing latitude.

Such a behaviour cannot be reproduced by the isotropic model (model 1), nor can it be reproduced by a plane-parallel galactic halo (model 2) (see e.g. Fig. 5, $b = 25°$ and $b = -25°$). To overcome this problem we introduce a galactic-longitude dependence to the model. We demonstrate that this is necessary by modeling the observations first with a simple linear dependence of the 3/4 keV intensity on galactic longitude, assuming a linear decrease of the 3/4 keV distant galactic component between $l = 0°$ and $l = 180°$.

Furthermore, we have to take into account that the amplitude of the intensity modulation decreases as latitude increases from the galactic equator to the galactic poles. As is obvious in Fig. 5, such a linear dependence of the 3/4 keV intensities on galactic longitude (thick lines in Fig. 4) reproduces the observed 3/4 keV count-rate distribution better than the models discussed above. It is also relevant that the dependence of the 3/4 keV

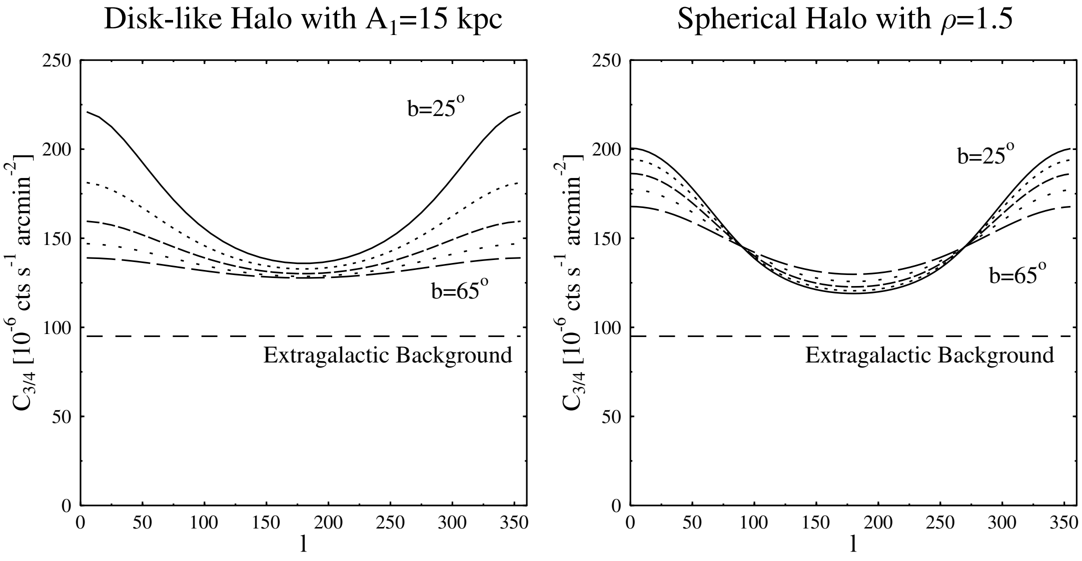

Fig. 5. Intensity variation of the 3/4 keV XRB predicted by the flattened-halo model (Sect. 5.2) with A_l = 15 kpc and h_z = 4.4 kpc (*left*) and by the spherical-halo model with a halo radius of $\rho = 1.5R_\odot$ (*right*). The 3/4 keV intensity variation is plotted against longitude for latitudes between $|b| = 25°$ and $|b| = 65°$. The intensity level of the extragalactic XRB is marked by the horizontal dashed line. Note that the intensity variation is not caused by photoelectric absorption of the interstellar matter along the line of sight, but represents the *unabsorbed* 3/4 keV XRB brightness.

radiation on galactic longitude is the same for both galactic hemispheres. This indicates that the brightness of the distant galactic XRB plasma is the same on both sides of the Galaxy.

Hence we conclude that a thermal X-ray halo model must fulfill the following conditions:

- The halo X-ray count rate modelled should decrease smoothly from the galactic center towards the galactic anticenter.
- The halo X-ray count rate should decrease smoothly from the galactic plane to the galactic poles.
- The halo model should be largely symmetric with respect to the galactic equator.

Recently Freyberg (1994, 1997) analyzed the 3/4 keV RASS data and came to the conclusion that a spherical-halo model (model 3) with $\rho \leq 3$ gives the best fit to the data. Indeed such a model (see Fig. 5 right) is consistent with the conditions mentioned above.

Another model which also accounts for the above conditions follows from analysis of the Leiden/Dwingeloo survey and describes the distribution of H I gas at large z distances. We explain this model first before comparing it with the spherical galactic halo model.

5.2. A halo hydrostatic-equilibrium model

Recent investigations by Kalberla et al. (1997) tentatively suggest the existence of H I at large z distances which can be described by hydrostatic equilibrium conditions between gravitation, gas pressure, and magnetic pressure. H I gas with a velocity dispersion of $\sigma \sim 60\,\mathrm{km\,s^{-1}}$ was found to be consistent with model assumptions of a turbulent gas layer with a scale height of 2 kpc or more. Such a high-dispersion H I halo agrees with the predictions of Boulares & Cox (1990) but is apparently in disagreement with models proposed by Spitzer (1956), Bloemen (1987), and Wolfire et al. (1995).

In the following, we assume that the galactic X-ray halo may be caused by a hot gas at a temperature of kT = 0.135 keV which is in hydrostatic equilibrium with the gravitational potential of the Galaxy. The pressure $p(z) = n(z)T(z)$ is assumed to balance the gravitational potential $\Phi(z)$:

$$n(R,z) = n_0 \cdot g_l(R) \cdot \exp(-120 \cdot \Phi(z)/T) \quad (8)$$

The function g_l according to Taylor & Cordes (1993) defines a volume-density gradient as function of galactocentric radius, R:

$$g_l(R) = \mathrm{sech}^2(R/A_l)/\mathrm{sech}^2(R_\odot/A_l) \quad (9)$$

where A_l is the radial scale length and $R_\odot$ = 8.5 kpc. Taylor & Cordes (1993) assumed a scale length of A_l = 20 kpc for the Reynolds (1991) layer. We used the potential $\Phi(z)$ derived by Kuijken & Gilmore (1989) which is in agreement with the potential derived by Bienaymé et al. (1987). Such a potential implies a low fraction of hidden mass in the Galactic disk (see Boulares & Cox 1990 and Crézé 1991). The normalization of the density n_0 is determined by the emission measure, $EM \propto \int n^+(z)^2 dz$ at $(l,b) \sim (90°, 60°)$, taken from the spectral-fitting results described in Sect. 3.

Most of the H I gas is confined at $|z| \leq 400$ pc (Dickey & Lockman 1990). Since in the spectral analysis the foreground plasma component is fit well by kT = 0.08 keV (Sect. 3), no 3/4

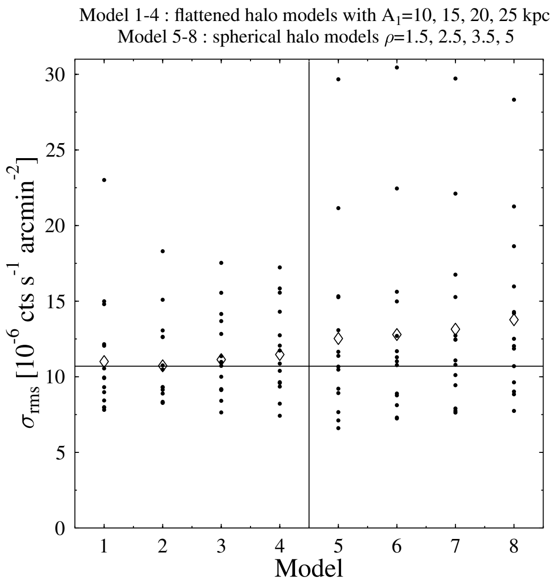

Fig. 6. Mean rms deviations ($\sigma_{\rm rms}$) between the $3/4$ keV RASS data and the different X-ray halo models evaluated for each latitude strip (Δb = 5°) from $|b|$ = 25° to 85° (smoothed to Δl = $2\overset{\circ}{.}5$). The first four models are thick-disk models with h_z = 4.4 kpc and A_l = 10, 15, 20, and 25 kpc, respectively; models 5 to 8 represent spherical-halo models with ρ =1.5, 2.5, 3.5, and 5, respectively. The diamond symbols mark the mean rms deviation averaged over all latitude strips. Obviously the mean rms deviations of flattened-halo models are in general smaller than those of the spherical halo models. The flattened-halo model with the lowest rms deviation is number 2, corresponding to A_l = 15 kpc.

keV emission is expected from the foreground component. Taking this observational result into account, we assumed that the hot gas causing the XRB is located entirely beyond $|z| > 400$ pc. Since our analysis is restricted to $|b| > 20°$ this assumption holds true for the local environment of the Sun and not for the entire galactic disk. Such an assumption affects the results of our modeling only to a minor degree, due to the necessary renormalization with respect to the observed emission measure towards the galactic poles. We found no evidence for any significant X-ray plasma temperature variation, hence we assume that the X-ray halo can be described by an isothermal distribution. In this case the X-ray halo temperature of kT = 0.135 keV (Sect. 3) corresponds to a scale height of h_z = 4.4 kpc.

In summary, the parameters needed for our model are: a temperature, kT = 0.135 keV; a mid-plane density, n_0, reproducing the observed emission measure, EM; and a scale length, A_l, which still has to be determined. The count rate dependence on galactic coordinates for a scale length of A_l = 15 kpc is drawn in Fig. 5 (*left*). Comparison with the count rate distribution of the spherical-halo model (Fig. 5, *right*) shows that both models reproduce the basic conditions mentioned in Sect. 5. The differences are found in the detailed l variations, as discussed in the following section.

5.3. Flattened-halo model versus spherical-halo model

To decide which model fits the $3/4$ keV X-ray data best, we calculated the rms deviations, $\sigma_{\rm rms}$, of the residual between observations and model for each smoothed galactic latitude strip (Fig. 6). For the flattened models we varied the scale-length parameter A_l between 10 kpc and 25 kpc, while the spherical-halo parameter ρ was varied between 1.5 and 5. The data-points with the largest deviations correspond to the latitude strips $|b|$ = 20° − 30°, where generally the largest deviations from our simple radiation transfer model are expected to occur in any case, because of the additional X-ray radiation from the galactic disk.

The spherical-halo models (Fig. 6) reveal in general a mean rms deviation (marked with diamonds in Fig. 6) larger than that of the flattened-halo models. Of the spherical-halo models, the one with a normalized radius of $\rho \approx 2 - 3$ appears to fit the observations best. This is roughly consistent with the result of Freyberg (1994, 1997) who determined $\rho \leq 3$ as best-fit value.

The flattened-halo models (Fig. 6, models $1-4$) have, however, generally lower mean rms deviations; the scatter between the different latitude strips is also significantly lower, indicating a systematically better fit of the observations by the flattened-halo models than is realized by the spherical-halo ones. The best-fit scale length is A_l = 15 kpc, similar to the scale length found for the flattened H I halo suggested by Kalberla et al. (1997).

For the preferred flattened X-ray halo model with A_l = 15 kpc we obtain an emission measure EM at the galactic poles of

$$EM(b = 90°) = 5 \cdot 10^{-3}\,\mathrm{pc\,cm^{-6}} \qquad (10)$$

with a mid-plane density of $n_0 = 1.3 \cdot 10^{-3}\,\mathrm{cm^{-3}}$ (Eq. 8). The resulting variations with longitude and latitude, expressed as $3/4$ keV count rates, are shown in Fig. 5 (*left*).

5.4. Comparison of the best-fit flattened-halo model with the observations

We have to modify Eq. (4) according to the results derived above, by introducing a functional dependence of $C_{3/4,\mathrm{MK}}$ on galactic coordinates:

$$\begin{aligned} C_{3/4}(l,b) \;=\; & C_{3/4,\mathrm{PL}}e^{-\sigma_{\mathrm{PL}}N_{\mathrm{HI}}} \\ & + C_{3/4,\mathrm{MK}}(l,b)e^{-\sigma_{\mathrm{MK}}N_{\mathrm{HI}}} \end{aligned} \qquad (11)$$

In Fig. 7 we show data from all analyzed latitude strips, smoothed to an angular resolution of Δl = $2\overset{\circ}{.}5$. The thin line within the upper part of each latitude panel represents the modelled $3/4$ keV count rate. The thick line in the lower half of the corresponding panel indicates the difference between model and observations. Especially the amplitude of the observed $3/4$ keV intensity variation is well reproduced in each latitude strip.

The largest deviations between observations and model, with $\Delta C_{3/4} \sim 25 \cdot 10^{-6}$ cts s^{-1} arcmin^{-2} , are located near the galactic plane ($|b| < 30°$) between l = 0° and 180°. Since

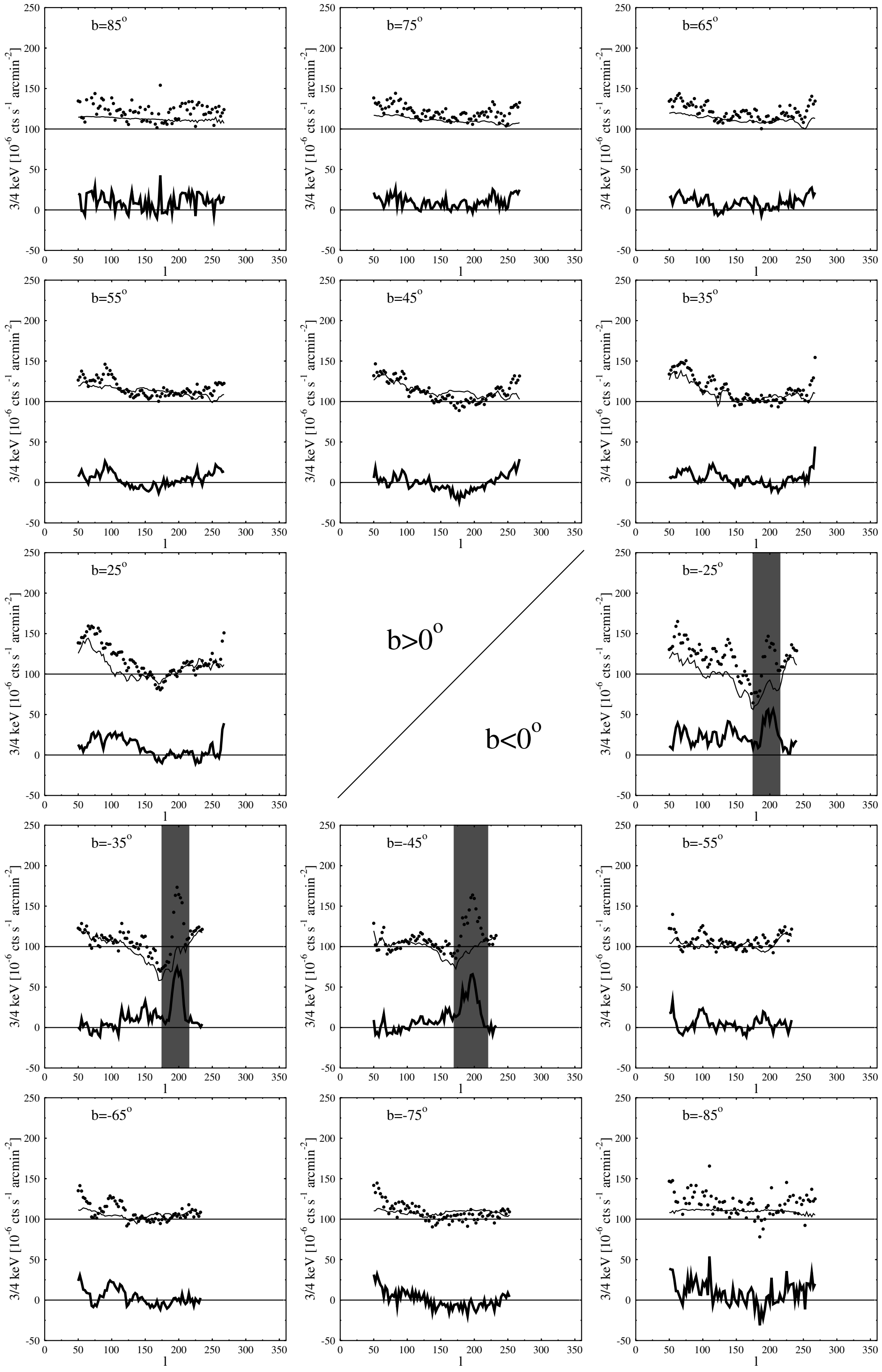

Fig. 7. Comparison of the 3/4 keV RASS data (points) with the count rates predicted by the flattened-halo model with $A_1 = 15$ kpc and $h_z = 4.4$ kpc (thin line). In the lower part of each panel the differences between data and model are plotted. The latitude strips cover a range of 10° centered at the latitude noted within each panel. The data are smoothed in longitude to 2.°5 angular resolution. In the southern galactic hemisphere the grey-shaded area indicates the Orion–Eridanus X-ray enhancements. The Loop I region, as well as the region of $\delta < -30°$ (where no adequate H I 21-cm line data are yet available) are excluded in this figure. In the ideal case that the observed and modelled 3/4 keV XRB intensity profiles would match each other perfectly, the thick line would show a white-noise response.

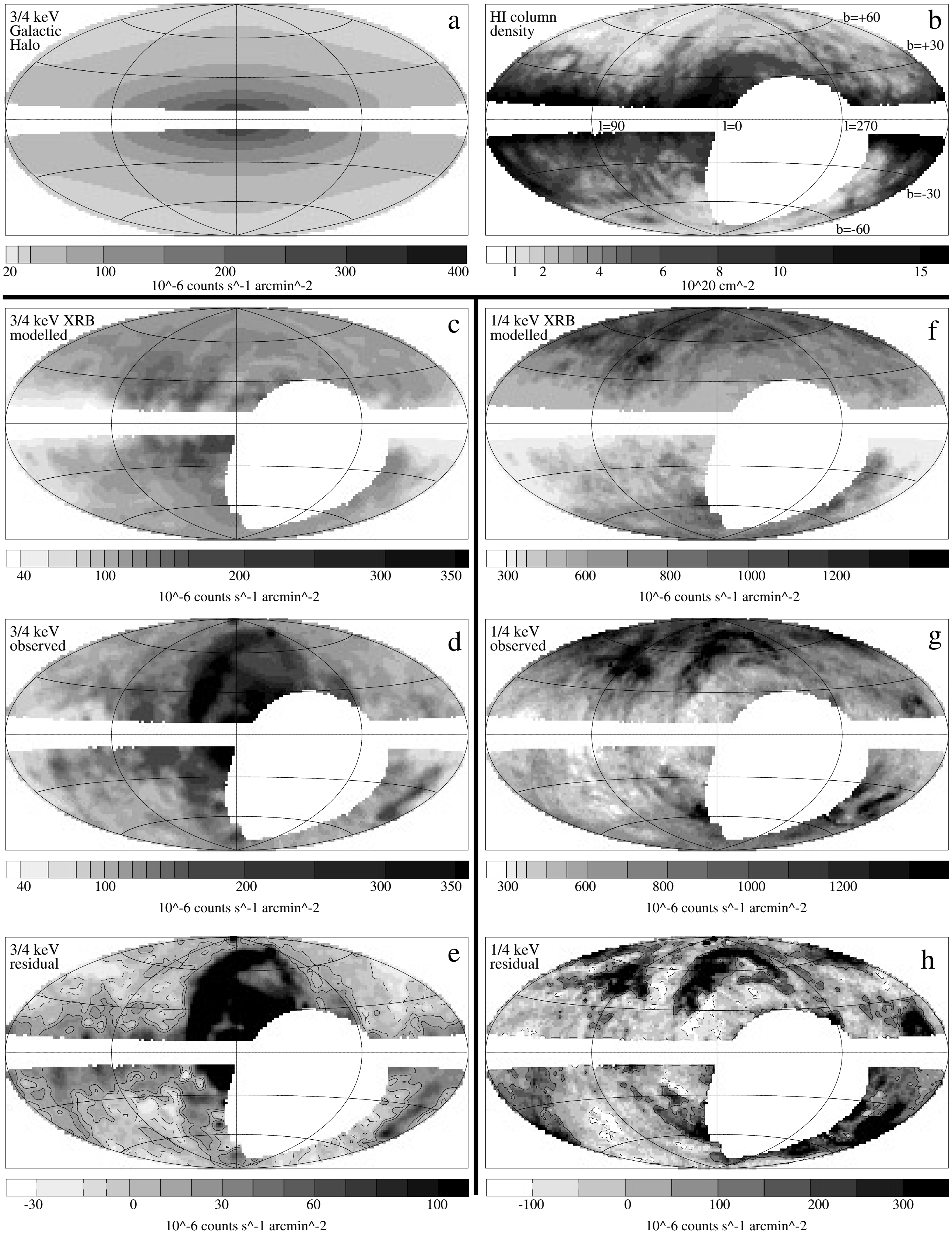

Fig. 8a–h. Explanations after Fig. 9.

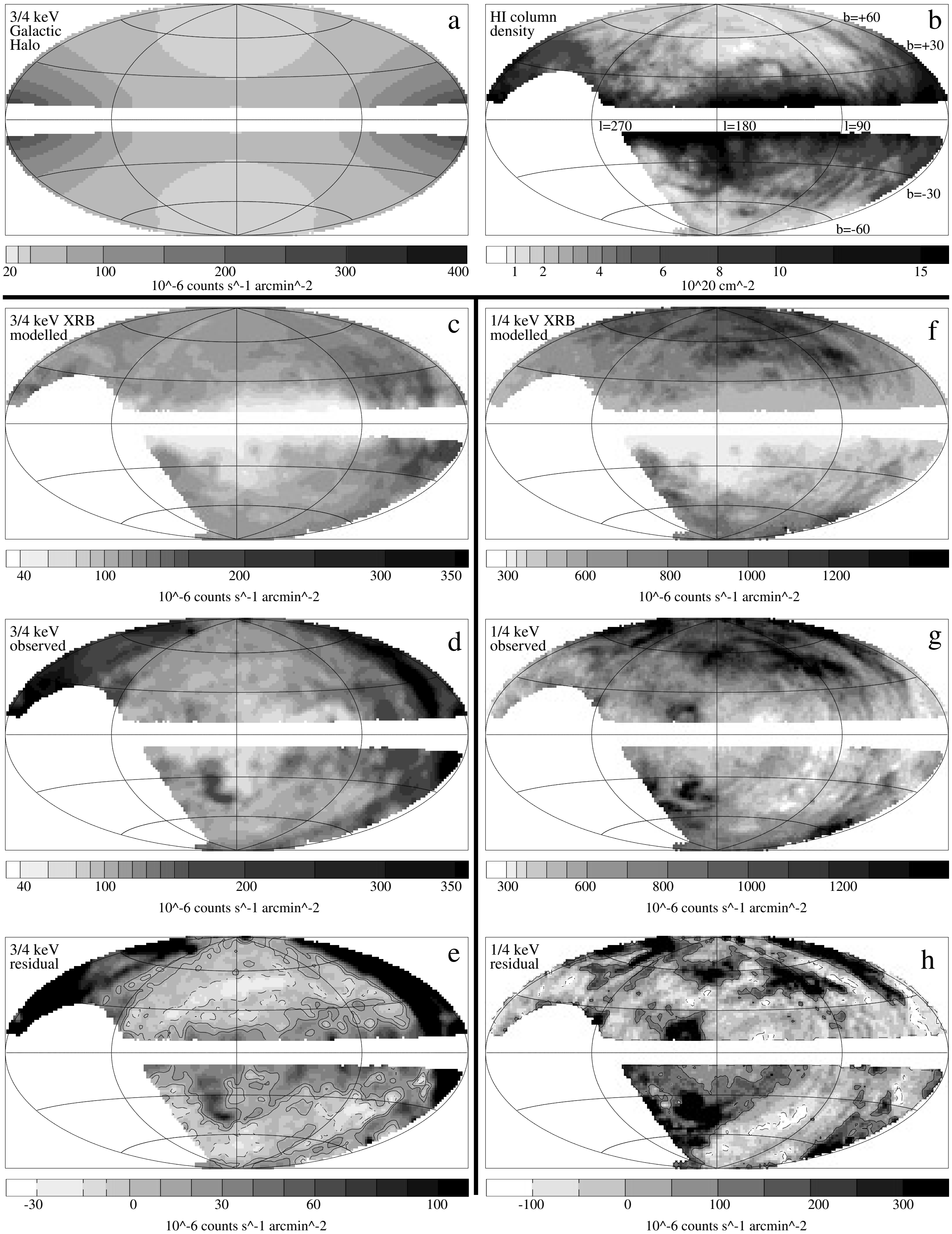

Fig. 9a–h. Explanations see next page.

Fig. 8a–h. Comparison of the modelled and observed 3/4 keV and 1/4 keV XRB maps centered on the galactic center in Hammer-Aitoff projection. The area within 10° of the galactic plane is blanked out. **a** Intensity distribution of the distant galactic X-ray plasma as predicted by the flattened X-ray halo model (A_1 = 15 kpc, h_z = 4.4 kpc) smoothed to an angular resolution of 5°. The count rates are normalized to the XRB intensities observed within the 3/4 keV energy range. To obtain the total unabsorbed diffuse XRB intensity the constant extragalactic XRB radiation has to be added to this map. **b** H I column density distribution as measured in the Leiden/Dwingeloo H I survey. The area close to the galactic equator is blanked, as is the area at $\delta < -30°$ not covered by the Leiden/Dwingeloo survey. The H I column density distribution quantitatively traces the X-ray absorbing interstellar matter which modulates the unabsorbed XRB intensity distribution shown in panel **a**. **c** Modelled 3/4 keV XRB following Eq. (11). This modelled 3/4 keV XRB distribution has to be compared with the observed XRB intensity distribution, shown in panel **d**. **e** Difference map showing observed minus the modelled XRB intensity distribution. The grey-scale coding is optimized to accentuate the differences between the modelled and observed XRB maps. Solid contour lines mark areas of too-low predicted X-ray intensities (10 and $20{\cdot}10^{-6}$ cts s^{-1} arcmin^{-2} levels); too-high predicted X-ray intensities ($-10{\cdot}10^{-6}$ cts s^{-1} arcmin^{-2} level) are indicated by dashed contour lines. The X-ray features contributing to the strong residuals are discussed in the text. **f** Modelled XRB intensity distribution of the 1/4 keV energy range smoothed to an angular resolution of 2.°5. The X-ray foreground intensities are given in Table 2. To calculate this figure we scaled the unabsorbed XRB map shown in panel **a** by a constant factor to the intensity level within the 1/4 keV energy range. This unabsorbed XRB intensity distribution is attenuated by the total H I column density distribution shown in panel **b**. Map **f** has to be compared quantitatively with the observed XRB map in panel **g**. **h** Difference map between the observed and modelled XRB intensity distribution. Solid contour lines enclose areas of too-low predicted X-ray intensities; dashed contour line encircle regions of too-high predicted X-ray intensities. The dominant features in the residual maps are Loop I and the Orion-Eridanus Bubble. The dynamic range of the difference maps is much smaller than those of the XRB maps, thus the modelled XRB intensity distributions fits the observational data well.

Fig. 9a–h. Comparison of the modelled and observed 3/4 keV and 1/4 keV XRB maps centered on the galactic anticenter in Hammer-Aitoff projection (cf. Fig. 8). **a** 3/4 keV intensity distribution of the distant galactic X-ray plasma as predicted by the flattened X-ray halo model (A_1 = 15 kpc, h_z = 4.4 kpc). **b** H I column density distribution derived from the Leiden/Dwingeloo H I survey. **c** Modelled 3/4 keV XRB intensity distribution, which has to be quantitatively compared with the observed XRB intensity distribution shown in panel **d**. The difference map representing observed minus modelled XRB intensities is shown in panel **e**. Solid contour lines mark areas of too-low predicted X-ray intensities ($10{\cdot}10^{-6}$ cts s^{-1} arcmin^{-2} and $20{\cdot}10^{-6}$ cts s^{-1} arcmin^{-2} levels); too-high predicted X-ray intensities ($-10{\cdot}10^{-6}$ cts s^{-1} arcmin^{-2} level) are indicated by dashed contour lines. **e** Modelled XRB intensity distribution of the 1/4 keV energy range. **g** Observed 1/4 keV intensity distribution. The difference between the observed and modeled X-ray intensity distribution is shown in panel **h**. Prominent in the 1/4 keV as well in the 3/4 keV difference maps are the Orion-Eridanus Bubble, located near $(l, b) \approx (200°, -45°)$, and the northern part of the "Monogem ring", located near (220°, +15°). Other residual X-ray features are discussed in the text.

$\Delta C_{3/4}$ is larger than zero, corresponding to too low predicted count rates, excess emission is located here.

Figs. 8 and 9, maps in Hammer-Aitoff projections centered on the galactic center and the galactic anticenter, respectively, demonstrate our results. These maps show the entire sky observed by the Leiden/Dwingeloo H I survey, but exclude the region of the galactic equator itself. The maps have been smoothed to an angular resolution of 5°. Patterns of excess emission at low latitudes are visible in the difference maps, panels (e), representing the observed-minus-modelled 3/4 keV distribution. The difference maps suggest that the excess emission X-ray features may be characteristically oriented perpendicular to the galactic plane, consistent with the existence of energetic events originating near the galactic disk and extending into the lower galactic halo. Certainly, one has to consider that the interstellar environment is more complex closer to the galactic plane. The radiation transport equation used, Eq. (11), may not represent this complex situation well.

Other enhanced residual-emission areas may be associated with X-ray features described in Sect. 4.2. The Orion-Eridanus Bubble is centered near $(l, b) = (200°, -40°)$; the enhancements near the galactic center are associated with Loop I and the galactic bulge. Comparison of the 3/4 keV and 1.5 keV RASS maps published by Snowden et al. (1995) reveal a rough correlation between 3/4 keV and 1.5 keV enhancements, suggesting the existence of an additional hot plasma component (kT > 0.14 keV) towards both Loop I and the Orion-Eridanus Bubble, as well as generally towards the galactic plane.

Extended areas where the predicted count rates are too high are observed at a level of $\Delta C_{3/4} \leq 10{\cdot}10^{-6}$ cts s^{-1} arcmin^{-2} in the smoothed latitude strips, e.g. in the strip b = 40° to 50° at l = 180° (Fig. 7). Comparing the residual maps in Figs. 8 and 9 with the survey exposure map shown by Snowden et al. (1995) indicates that these deviations may be attributed to the instrumental scanning direction of the RASS (see the 3/4 keV map by Snowden et al., 1995).

In view of the above, we conclude that our flattened-halo model with h_z = 4.4 kpc and A_1 = 15 kpc can reproduce the observed 3/4 keV RASS data down to the present accuracy limit of the X-ray data. Additional emission close to the galactic plane may be caused by localized galactic features.

6. The 1/4 keV X-ray background

The flattened-halo model of the 3/4 keV RASS energy band is based on physical considerations which constrain important properties of the 1/4 keV XRB radiation. In particular, the derived temperature of the galactic halo thermal plasma (kT = 0.13–0.14 keV) is a sensitive function of the intensity ra-

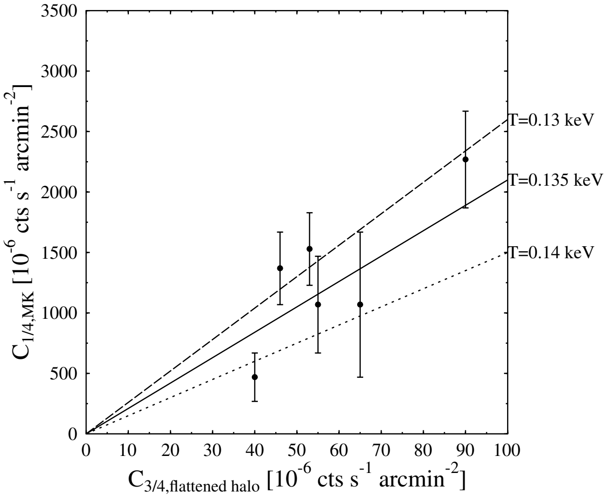

Fig. 10. XRB 1/4 keV intensities, extracted from the analyses of Herbstmeier et al. (1995) and of Kerp et al. (1997), plotted versus the 3/4 keV count rates predicted by the flattened-halo model. The contribution of the extragalactic XRB has been subtracted from the 1/4 keV data. The linear correlation between the 1/4 keV and modelled 3/4 keV data suggests that the source intensity distributions are equal for both X-ray energy ranges. The dotted, solid, and dashed lines represent different kT values, indicating a narrow plasma temperature range which can account for a simultaneous fit of the 1/4 keV and the 3/4 keV data. This diagram supports our spectral-fit results (Fig. 1) as well as the zero-order assumption of an isothermal galactic X-ray halo.

Table 2. Foreground count rates $C_{\rm fg}$ used to calculate the 1/4 keV XRB intensity distribution plotted in panels (f) of Figs. 8 and 9.

b [°]	Count rate $C_{\rm fg}$ [10^{-6} cts s^{-1} arcmin^{-2}]
> 60	550
30 to 60	450
20 to 30	400
-30 to -20	300
-50 to -30	300
< -50	350

tio between the 3/4 keV and 1/4 keV XRB radiation. Therefore, we demonstrate the validity of our 3/4 keV galactic X-ray halo model by the *extrapolation* to the 1/4 keV XRB.

One has to take into account that roughly half of the observed 1/4 keV radiation is caused by local (within, say, 100 pc) X-ray emission (McCammon & Sanders 1990). Within the low-volume-density environment of the Sun, the local interstellar medium is distributed inhomogeneously (Frisch 1995). Welsh et al. (1991) found that beyond a distance of 50 pc the interstellar medium cannot be regarded as a local cavity of regular shape. In consequence, the foreground X-ray emission term in the X-ray radiation-transport equation cannot be regarded as constant across the entire sky; thus a more a careful radiation-transport analysis for the 1/4 keV band is called for. Such an analysis was recently performed towards selected fields by Herbstmeier et al. (1995), Kerp et al. (1996, 1997). We used their values of the galactic-halo intensity in the 1/4 keV energy range and compare these values with our modelled 3/4 keV count rates. As mentioned above, this test constrains the temperature interval of the galactic halo plasma. In the case that the 3/4 keV and the distant 1/4 keV diffuse galactic X-ray emission can be attributed to the same plasma we have to find a linear correlation between both intensity distributions.

First, we evaluate the extragalactic XRB intensity in the 1/4 keV band. Using the spectral fitting results discussed in Sect. 3, the extragalactic XRB contribution to the 1/4 keV count rate can be estimated as $C_{1/4,\rm extra} \sim 230 \pm 30{\cdot}10^{-6}$ cts s^{-1} arcmin^{-2} . This value is in quantitative agreement with the extragalactic 1/4 keV XRB intensity values determined by the analysis of shadowing galaxies carried out by Barber et al. (1996). Second, we subtract this extragalactic XRB count rate from the 1/4 keV XRB count rate determined by Herbstmeier et al. (1995) and by Kerp et al. (1996, 1997). Third, we plot these modified 1/4 keV intensities against the 3/4 keV count rates derived from the flattened-halo model. Fig. 10 shows that, indeed, the 3/4 keV count rate of the galactic halo is linearly correlated with the distant 1/4 keV XRB count rate. This result indicates that the 3/4 keV and the distant 1/4 keV XRB have the same source distribution. Indicated by the solid, dashed, and dotted lines in Fig. 10 are different plasma temperatures ranging only from k$T = 0.13$ to 0.14 keV. This narrow temperature range is in agreement with the PSPC spectral-fitting results of Sect. 3.

These findings suggest that a significant fraction of the 3/4 keV and 1/4 keV XRB radiation is caused by thermal-plasma emission originating in the galactic halo.

6.1. Modeling the 1/4 *keV sky*

To validate the above suggestion further, we scaled the 3/4 keV X-ray halo intensity distribution to the 1/4 keV energy range and cross-correlated the modelled XRB intensity distribution with the observed one. The angular resolution of the RASS data is not sufficient to allow a detailed 1/4 keV X-ray transport analysis: the 2° angular resolution results in the small-scale structure of the X-ray attenuating interstellar medium being smeared out.

To determine the foreground intensity distribution we subtracted a modelled 1/4 keV X-ray halo XRB map from the observed RASS 1/4 keV map. For each latitude range we evaluated a constant foreground intensity (cf. Table 2), representing the minimum offset between the modelled halo and the observed 1/4 keV distribution. Using the flattened X-ray halo model and a plasma temperature of k$T = 0.135$ keV and with the constant foreground count rate tabulated in Table 2, we evaluated a second 1/4 keV XRB intensity distribution (see panels (f) of Figs. 8 and 9) which has to be compared with the observed XRB intensity distribution shown in panels (g) of Figs. 8 and 9. Although the observed 1/4 keV count rate is dominated by the foreground contribution, we expect that, especially on smaller angular scales, photoelectric absorption of the XRB components produces the observed 1/4 keV count rate variations.

Utilizing the H I column density maps shown in panels (b) of Figs. 8 and 9, it is possible to identify several areas where the modelled XRB map reproduces the observed $1/4$ keV distribution particularly well. These regions include that of the the inner side of the north celestial pole loop near $(l, b) \sim (135°, 35°)$, as an X-ray bright spot; the high-density region near $(l, b) \sim (150°, -70°)$, as absorption; the low-density region near $(l, b) \sim (90° - 150°, -60°$, as a bright band; and the complex absorption pattern near $(l, b) \sim (240°, 50°)$. Even the Lockman hole region near $(l, b) \sim (150°, 50°)$ is well reproduced.

Although we have neglected a longitude variation of the foreground component, the difference maps (observed minus modelled XRB) shown in panels (h) of Figs. 8 and 9 reveal only two areas other than the excess X-ray emission associated with Loop I and the "Monogem Ring" ($l \sim 220°, b \sim +15°$), which have $\Delta C_{1/4} \geq +200{\cdot}10^{-6}$ cts s^{-1} arcmin^{-2} in the northern hemisphere; other northern regions are characterized by deviations between observation and model between $[-75 \leq \Delta C_{1/4} \leq 75]{\cdot}10^{-6}$ cts s^{-1} arcmin^{-2} . These two regions with a deficit of predicted $1/4$ keV emission coincide with the positions of two HVC complexes, namely complex C, near $(l, b) \sim (100°, 40°)$ (see Kerp et al. 1996), and complex M, near $\sim (180°, 60°)$ (see Herbstmeier et al. 1995). The brightest spot of complex M is centered near the HVC cloud M III, which is also detectable in the $1/4$ keV maps shown by Herbstmeier et al. (1995). Since these enhancements towards the two HVC complexes is also visible in the residual map of the X-ray radiation-transport analysis by Marshall & Clark (1984) instrumental effects can be excluded for the *ROSAT* data. In contrast to the $1/4$ keV situation, the $3/4$ keV residual map reveals no significant excess emission close to the two HVC complexes C and M.

The $1/4$ keV residual emission in the southern hemisphere can be divided into two parts. At $l > 160°$, the predicted count rate is too low ($\Delta C_{1/4} \sim 250{\cdot}10^{-6}$ cts s^{-1} arcmin^{-2}); at $l < 160°$, the predictions are too high ($\Delta C_{1/4} \sim -100{\cdot}10^{-6}$ cts s^{-1} arcmin^{-2}). Since this behaviour is not positionally correlated with any distinct H I structure and a similar residual feature is not visible in $3/4$ keV data, this behaviour is not produced by the X-ray transport solution. It may be caused by a variation within the foreground X-ray emission or by a dependence of absorption on galactic longitude, e.g. by a large-scale inhomogeneity in the low-volume-density surroundings of the Sun. But since the distribution of this deviation in the southern hemisphere at $l < 160°$ is parallel to the scanning direction of the RASS data, a residual effect of the RASS data reduction cannot be excluded.

Despite the problem of the unknown distribution of foreground emission, the halo model appears to be applicable to the $3/4$ keV band as well as to the $1/4$ keV bands, down to the accuracy limit of the RASS X-ray data.

In our hydrostatic model the X-ray halo emission is symmetric with respect to the galactic plane (the Sun's z-offset from the plane is negligible compared to h_z = 4.4 kpc). In the $1/4$ keV band the *observed* X-ray count rates toward both galactic poles differ significantly (see Fig. 9g). Snowden (1997) concludes that this is due to a higher intensity of the unabsorbed X-ray halo emission in the northern galactic hemisphere. Our analysis suggests that the observed north/south asymmetry is caused by the photoelectric absorption of the foreground gas traced by the H I emission in addition to an asymmetry in the 1/4 keV foreground intensity.

7. Summary

We analyzed the $3/4$ keV and $1/4$ keV *ROSAT* all-sky-survey data and evaluated the photoelectric absorption of the neutral matter traced by H I gas as given by the Leiden/Dwingeloo survey. The main results are:

1. At high latitudes near $(l, b) \sim (90°, 60°)$ the temperature of the distant X-ray MK plasma is kT = 0.13–0.14 keV (Sect. 3.2), a value in agreement with other published X-ray temperatures obtained towards different directions of the galactic sky. Hence, we found that the thermal X-ray component is, in a first approximation, isothermal.
2. The photoelectric-absorption-corrected $3/4$ keV count rate decreases with increasing latitude and towards the galactic anticenter, (Sect. 3.5), indicating that a significant fraction of the galactic $3/4$ keV emission originates in the halo.
3. We modelled an isothermal flattened X-ray halo based on hydrostatic equilibrium considerations (Sect. 4.1). An X-ray halo component with a scale height of h_z = 4.4 kpc and a radial scale length of A_1 = 15 kpc in addition to an extragalactic power-law ($\Gamma = -1.4$) component – both absorbed by galactic neutral matter – can reproduce the $3/4$ keV RASS data down to its data accuracy limit (Sect. 4.2).
4. The RASS $1/4$ keV large-scale intensity distribution is consistent with this X-ray plasma halo model (Sect. 6).

(Since our analysis is restricted to latitudes above $|b| > 20°$ and to directions away from the galactic bulge, we note that our results are largely restricted to information contributed from a volume within about 4 kpc from the Sun.)

Finally, assuming that the X-ray halo model is valid for the entire Galaxy, we obtain a total halo X-ray luminosity of $L_X \sim 7 \cdot 10^{39}$ erg s^{-1}. This value is comparable to luminosities found for the X-ray halos of M51 and NGC1566 by Ehle (1996). This may be an indication of a common X-ray halo-producing mechanism, as for example a galactic fountain by stellar activity (e.g. Bregman 1980), where hot material is transported up and radially outward, reproducing the X-ray parameters determined.

Acknowledgements. J. Pietz thanks the Deutsche Agentur für Raumfahrtangelegenheiten for support under the grant No. 40012 and J. Kerp thanks the Deutsche Forschungsgemeinschaft for support under the grant No. ME 745/17-2. We are grateful to K.S. de Boer and an anonymous referee for helpful comments.

References

Almaini O., Shanks T., Boyle B.J., Griffiths R.E., Roche N., et al., 1996, MNRAS 282, 295

Barber C.R., Roberts T.P., Warwick R.S., 1996, MNRAS 282, 157

Berkhuijsen E.M., 1971, A&A 14, 359
Bienaymé O., Robin A.C., Crézé M., 1987, A&A 180, 94
Bloemen J.B.G.M., 1987, ApJ 322, 694
Boulares A., Cox, D.P., 1990, ApJ 365, 544
Brown A.G.A., Hartmann D., Burton W.B., 1995, A&A 300, 903
Bregman J.N., 1980, ApJ 236, 577
Bruhweiler F.C., 1996, The Morphology and Physics of the Local Interstellar Medium. In: Bowyer S. & Malina R.F. (eds.) Astrophysics in the Extreme Ultraviolet. Kluwer Academic Press, p.261
Crézé M., 1991, The Galactic Gravitational Potential. In: Bloemen H. (ed.) Proc. IAU Symp. 144, The Interstellar Disk-Halo Connection in Galaxies, Kluwer Academic Publishers, p.313
Danly L., Albert C.E., Kuntz K.D., 1993, ApJ 416, L29
Dickey J.M., Lockman F.J., 1990, ARA&A 28, 215
Egger R.J., Aschenbach B., 1995, A&A 294, L25
Ehle M., 1996, Halos of Nearby Spiral Galaxies. In: Zimmermann H.U., Trümper J.E., Yorke H. (eds.) Röntgenstrahlung from the Universe, MPE-Report 263, 371
Fabian A.C., Barcons X., 1992, ARA&A 30, 429
Freyberg M., 1994, Ph.D. thesis, University of Munich
Freyberg M., 1997, The Large-Scale Structure of the X-ray Halo. In: Lesch H., Dettmar R.-J., Mebold U., Schlickeiser R. (eds.) Proceedings of 156. WE-Heraeus-Seminar on The Physics of Galactic Halo, Akademie Verlag Berlin, p. 117
Frisch P.C., 1995, Space Sci. Rev. 72, 499
Gendreau K.C., Mushotzky R., Fabian A.C., et al., 1995, PASJ 47, L5
Guo Z., Burrows D.N., Sanders W.T., Snowden S.L., Penprase B.E., 1995, ApJ 453, 256
Hartmann, D. 1994, Ph.D. thesis, University of Leiden
Hartmann D., Kalberla P.M.W., Burton W.B., Mebold U., 1996, A&AS 119, 115
Hartmann, D. & Burton, W.B., 1997, Atlas of Galactic Neutral Hydrogen, Cambridge University Press
Hasinger G., Burg R., Giacconi R., et al., 1993, A&A 275, 1
Heiles C., Reach W.T., Koo B.-C., 1988, ApJ 332, 313
Herbstmeier U., Mebold U., Snowden S.L., et al., A&A 298, 606
Herbstmeier U., Kalberla P.M.W., Mebold U., et al., 1996, A&AS 117, 497
Kalberla, P.M.W., Westphalen, G., Mebold, U., Hartmann, D. & Burton, W.B 1997, A&A submitted
Keenan F.P., Shaw C.R., Bates B., Dufton P.L., Kemp S.N., 1995, MNRAS 272, 599
Kerp J., 1994, A&A 289, 598
Kerp J., Mack K.-H., Egger R., et al., 1996, A&A 312, 67
Kerp J., Pietz J., 1996, The Soft X-ray Radiation Transfer within the Interstellar Medium. In: Zimmermann H.U., Trümper J.E., Yorke H. (eds.) Röntgenstrahlung from the Universe, MPE-Report 263, 329
Kerp J., Burton W.B., Egger R., et al., 1997, A&A submitted
Kuijken K., Gilmore G., 1989, MNRAS 239, 605
Lachiže-Rey M., Asséo E., Cesarsky C.J., Pellat R., 1980, ApJ 238, 175
Lockman F.J., Gehman C.S., 1991, ApJ 382, 182
Magnani L., Hartmann D., Speck B.G., 1996, ApJS 106 447
Marshall F.J., Clark G.W., 1984, ApJ 287, 633
McCammon D., Burrows D.N., Sanders W.T., Kraushaar W.L., 1983, ApJ 269, 107
McCammon D., Sanders W.T., 1990, ARA&A 28, 657
Mewe R., Gronenschild E.H.B.M., van den Oord G.H.J., 1985, A&AS 62, 197
Morrison R., McCammon D., 1983, ApJ 270, 119
Nousek J.A., Fried P.M., Sanders W.T., Kraushaar W.L., 1982, ApJ 258, 83
Pickelner S.B., 1953, Doklady AS USSR 88, 229
Plucinsky P.P., Snowden S.L., Briel U.G., Hasinger G., Pfeffermann E., 1993, ApJ 418, 519
Reach W.T., Koo B.-C., Heiles C., 1994, ApJ 429, 672
Reynolds R.J., 1991, Ionized Disk/Halo Gas: Insight form optical emission lines and pulsar dispersion measures. In: Bloemen H. (ed.) IAU Symp. 144, The Interstellar Disk-Halo Connection in Galaxies, Kluwer Academic Publishers, p.67
Rocchia R., Arnaud M., Blondel C., et al., 1984, A&A 130, 53
Roche N., Griffiths R.E., Della Ceca R., et al., 1996, MNRAS 282, 820
Schwarz U., Wakker B.P., van Woerden H., 1995, A&A 302, 364
Sidher S.D., Sumner T.J., Quenby J.J., Gambhir M., 1996, A&A 305, 308
Snowden S.L., McCammon D., Burrows D.N., Mendenhall J.A., 1994, ApJ 424, 714
Snowden S.L., Hasinger G., Jahoda K., et al., 1994b, ApJ 430, 601
Snowden S.L., Freyberg M.J., Plucinsky P.P., et al., 1995, ApJ 454, 643
Snowden S.L., 1997, IAU Coll. 166 "The Local Bubble and Beyond", eds: Breitschwerdt D., Freyberg M., in press
Soltan A.M., Hasinger G., Egger R., Snowden S., Trümper J., 1996, A&A 305, 17
Spitzer L., 1956, ApJ 124, 20
Taylor J.H., Cordes J.M., 1993, ApJ 411, 674
Wakker B.P., van Woerden H., 1997, ARA&A 35, 217
Welsh B.Y., Vedder P.W., Vallerga J.V., Craig N., 1991, ApJ 381, 462
Wolfire M.G., McKee C.F., Hollenbach D., Tielens A.G.G.M., 1995, ApJ 453, 673
Zimmermann U., Becker W., Belloni T., et al., 1997, MPE-Report

This article was processed by the author using Springer-Verlag LaTeX A&A style file *L-AA* version 3.